

Midcrustal Thrusting and Vertical Deformation Partitioning Constraint by 2017 M_w 7.3 Sarpol Zahab Earthquake in Zagros Mountain Belt, Iran

by Ying-Hui Yang, Jyr-Ching Hu, Ali Yassaghi, Min-Chien Tsai, Mehdi Zare, Qiang Chen, Ze-Gen Wang, Ali M. Rajabi, and Farnaz Kamranzad

ABSTRACT

We investigate the geodetic data set of Interferometric Synthetic Aperture Radar (InSAR) including Advanced Land Observation Satellite (ALOS)-2 and Sentinel-1A/1B satellites for inferring the fault model of the 2017 M_w 7.3 Sarpol Zahab, Iran, earthquake. The InSAR deformation fields show that the seismogenic fault does not reach the ground surface, but some shallow folds have been triggered by the mainshock. Our preferred faulting model suggests that the coseismic rupture occurs on a single planar fault surface with a strike angle of 337.5°. Two significant slip sources are determined by the geodetic data: one is located within the 11.8- to 13.5-km depth range with a peak slip of 4.9 m, and the other occurs at the shallower depth (10.5–12.5 km) with a peak slip of 4.5 m. Both of them are responsible for the primary deformation signals in the geodetic imagery. The significant fault slip concentrates at the 10- to 14-km depth within the Pan-African basement. However, most of the aftershocks have depths between 3 and 12 km in the shallow sedimentary section. We hypothesize that the Hormuz Salt section with a depth of 12–13 km detaches the high-slip zones from the aftershock cluster, by which the fault slip is not transferred through the intervening salt section to the surface. The predicted static Coulomb stress change by our preferred faulting model at a depth of 10 km could encourage the occurrence of aftershocks. Moreover, the triggered fault-related folding in the southwest of the seismic zone has a positive Coulomb stress change and aseismic slip caused by the mainshock.

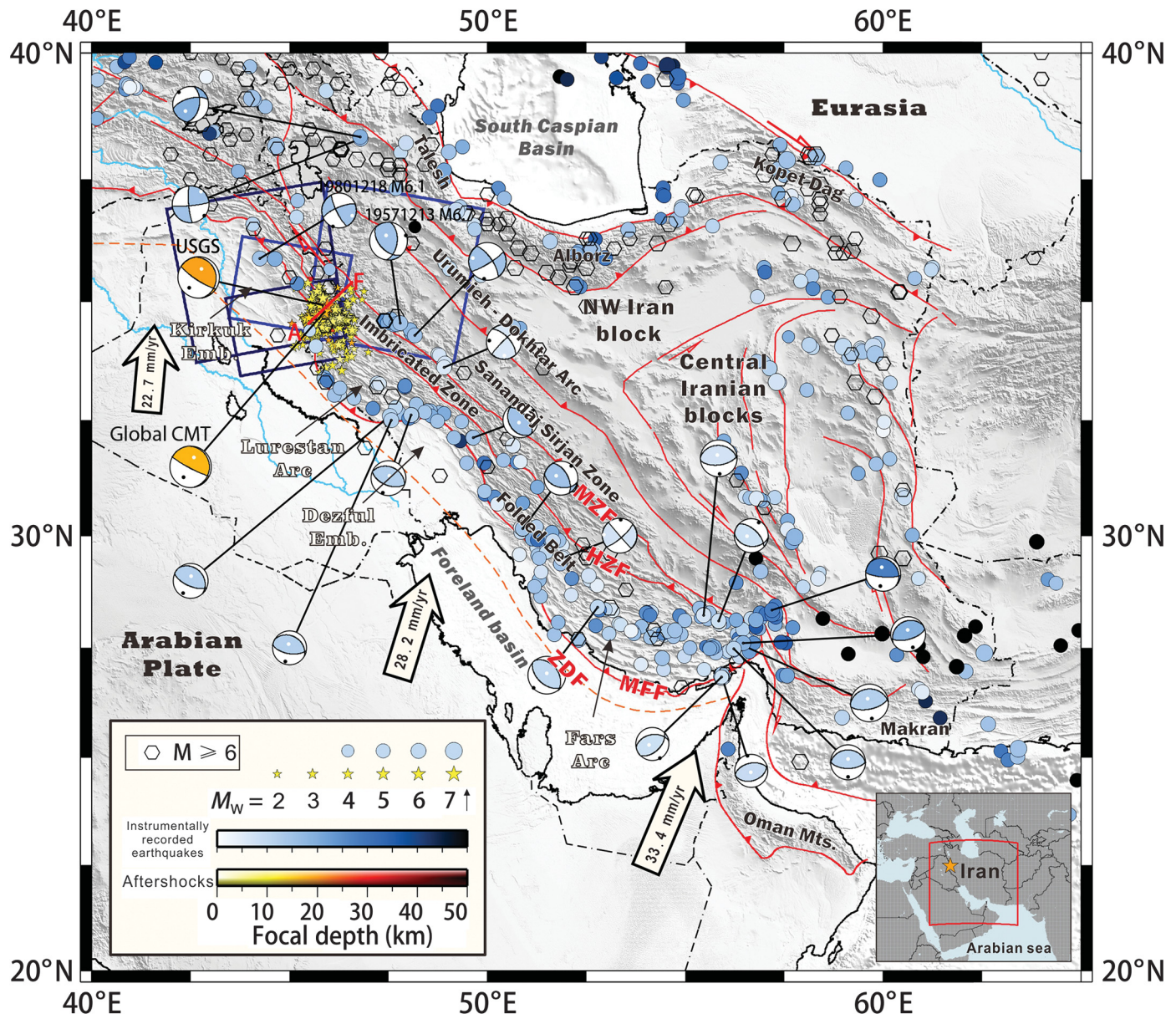
Electronic Supplement: Figures showing the geological and geo-dynamic map of the Zagros orogeny in the northwest Iran, the inferred curved faulting model of the 2017 Sarpol Zahab earthquake, and Interferometric Synthetic Aperture Radar (InSAR) interferograms.

INTRODUCTION

On 12 November 2017, the M_w 7.3 Sarpol Zahab earthquake struck northwest Iran near the border with Iraq, with the

epicenter (34.902° N and 45.952° E, U.S. Geological Survey [USGS] solution) roughly ~120 km northwest of city of Kermanshah. This strong earthquake caused severe surface shaking and building collapse, and it killed more than 400 and injured ~8000 people (Zare *et al.*, 2017). The Sarpol Zahab earthquake occurred at the northwest Zagros Mountain belt, and it might be associated with the rupture of the Zagros Mountain front fault (MFF) in Pol-e-Zahab Region (Zare *et al.*, 2017). The Zagros mountain range is a part of the Alpine-Himalaya mountain chain formed from the oblique collision between the Arabian and Eurasian plates during the closure of the Neo-Tethys Ocean (Berberian and King, 1981; Talbot and Alavi, 1996; Stampfli and Borel, 2002). The long-term geodetic observation in this zone shows that the convergence rate is ~28.0 mm/yr (Fig. 1; Sella *et al.*, 2002; Vernant *et al.*, 2004; DeMets *et al.*, 2010), and it accommodates almost half of the present-day shortening between the Arabian and Eurasian plates (Vernant *et al.*, 2004). The Zagros orogenic belt is characterized by an ~12-km-thick sedimentary cover, an ~2-km-thick Hormuz Salt section, and the Precambrian Arabian basement (McQuarrie, 2004). However, there are arguments about the presence of Hormuz Salt layer in the northern Zagros in which the basal décollement mainly consists of shale rather than salt (McQuarrie, 2004; Sherkati and Letouzey, 2004; Casciello *et al.*, 2009). McQuarrie (2004) and Sherkati and Letouzey (2004) suggest that a thick viscous layer at the base of the sedimentary cover in the Lorestan region is Hormoz salt or its equivalents. The previous studies show that most of the earthquakes occurs at a depth of 10–25 km under the Hormuz salt section (Berberian and Yeats, 2001; Engdahl *et al.*, 2006; Barnhart and Lohman, 2013). These geodetically imaged earthquakes rarely rupture to the surface (Jackson and Fitch, 1981; Berberian, 1995; Barnhart and Lohman, 2013), and the shallow slip is replaced by the folding that has caused the development of anticlines and synclines in this zone (Engdahl *et al.*, 2006; Nissen *et al.*, 2011).

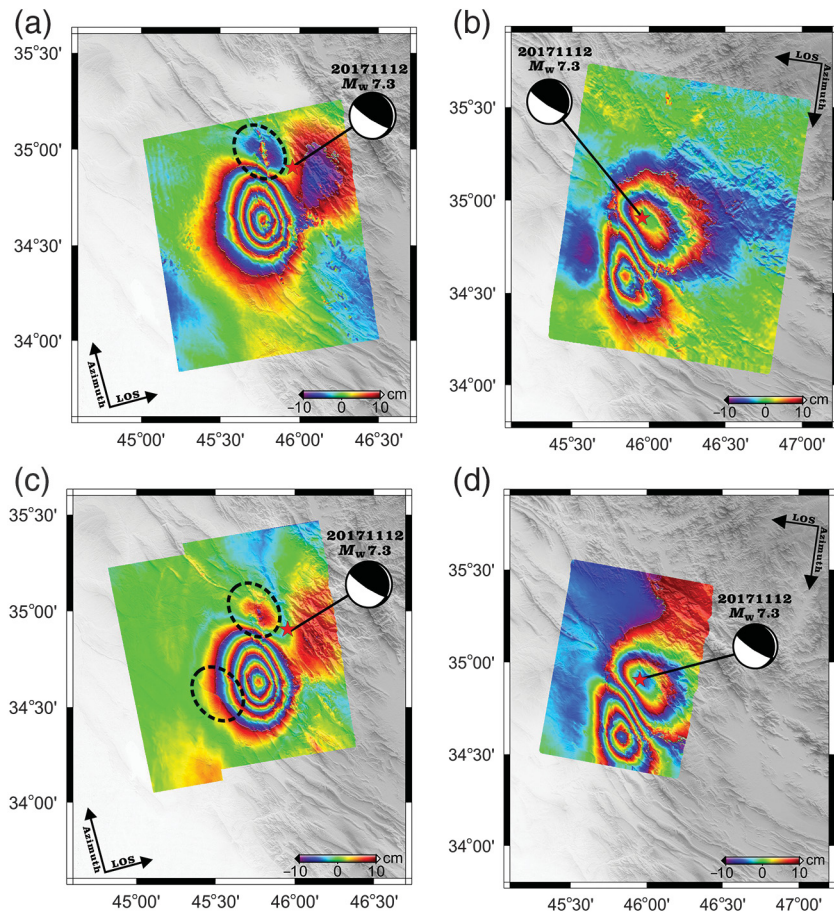
The northwest-trending Zagros orogenic belt is divided into five different tectonic domains from south (foreland) to



▲ Figure 1. Tectonic framework, background seismicity, and Sarpol Zahab earthquake sequences are mapped on a shaded relief of Shuttle Radar Topography Mission v.4 (SRTM-4) digital elevation model (Farr *et al.*, 2007), and the inset at the bottom right corner shows the interest range of this study. Warm color tone coded with focal depth represents the Sarpol Zahab earthquake sequences; the cool color tone coded with focal depth represents the background seismicity (Talebian and Jackson, 2004; Engdahl *et al.*, 2006). Black hexagons are the instrumentally recorded earthquakes with magnitudes greater than 6. White arrows with numbers are plate convergence rate between the Arabian and Eurasian plates (DeMets *et al.*, 2010). Red lines indicate the major structure and faults (Casciello *et al.*, 2009; Vegrés *et al.*, 2011). The red solid line marked by AF shows the surface trace of the geologic section (Sadeghi and Yassaghi, 2016). The two large blue solid rectangles denote the coverages of the Advanced Land Observation Satellite (ALOS)-2 ascending and descending tracks, and the two small blue solid rectangles indicate the coverages of the Sentinel-1 ascending and descending tracks. Blue solid rectangles denote the coverages of the ALOS-2, Sentinel-1 ascending and descending tracks, respectively. ZDF, Zagros deformation front; MFF, Mountain front fault; HZF, high Zagros fault; MZF, Main Zagros fault; Global CMT, Global Centroid Moment Tensor.

north (hinterland) (Fig. 1): the Mesopotamian–Persian Gulf foreland basin, the Folded belt zone, the imbricate zone (also called high Zagros thrust belt or Crush zone), the metamorphic and magmatic Sanandaj–Sirjan zone, and the Urumieh–Dokhtar Magmatic arc (Alavi, 2007). These tectonic domains are separated by major faults such as Zagros

deformation front (ZDF), MFF, high Zagros fault (HZF), and Main Zagros fault (MZF). The Sarpol Zahab earthquake occurred in the northwest part of the Folded belt zone between the MFF and HZF. It is the largest event striking the northwest Zagros folding belt in the past 200 yrs (Engdahl *et al.*, 2006).



▲ Figure 2. The Interferometric Synthetic Aperture Radar (InSAR) deformation fields of the 2017 Sarpol Zahab earthquake derived from ALOS-2 and Sentinel-1 Synthetic Aperture Radar images. One color cycle from violet to red indicates surface motion of 20 cm along satellite Line of Sight (LoS) direction. (a) ALOS-2 ascending, (b) ALOS-2 descending, (c) Sentinel-1 ascending, and (d) Sentinel-1 descending InSAR deformation. The red star indicates the epicenter of the 2017 Sarpol Zahab earthquake, and the black dashed ellipses denote the areas with significant fringes discontinuities.

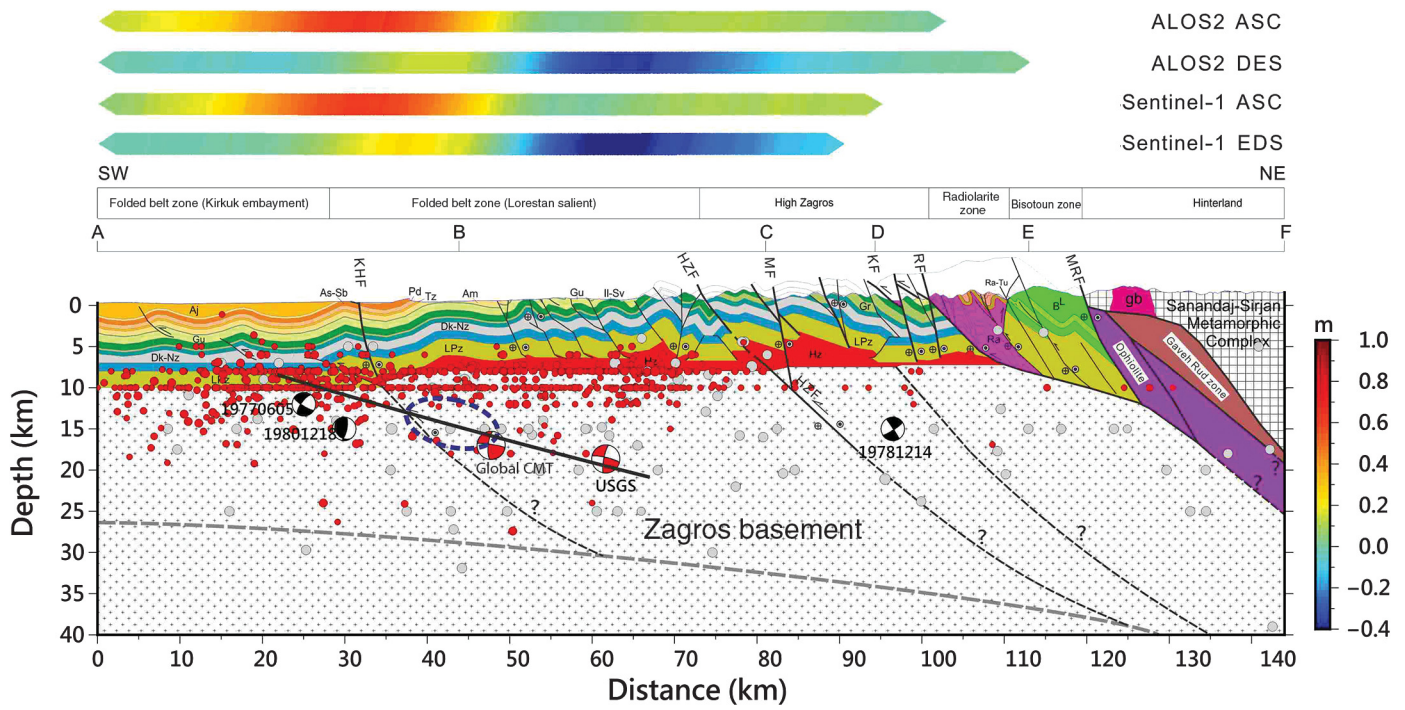
The focal mechanism derived from seismic waveform data by USGS (see [Data and Resources](#)) suggests that the mainshock is mainly a northwest-trending oblique-thrust faulting with shallow dipping to northeast at the midcrustal depth (19 km). However, the aftershocks within one month of the Sarpol Zahab earthquake mainly occur at 3- to 12-km depth ([Tatar and Yamini-Fard, 2017](#)). The ~10-km separation between the aftershocks cluster and earthquake centroid has caused some confusions, namely (1) whether the fault rupture has propagated to the ground surface, (2) how the slip distributes in this event, and (3) what are the Coulomb stress change caused by the mainshock in the seismic zone, which are also the main objectives of this study.

Here, we first acquire the coseismic Interferometric Synthetic Aperture Radar (InSAR) deformation fields using both the ascending and descending Advanced Land Observation Satellite (ALOS)-2, Sentinel-1 Synthetic Aperture Radar (SAR) images. Then we characterize the possibility of the seismogenic fault rupturing to the ground surface using the InSAR deformation fields. Furthermore, we invert the InSAR deformation data to determine the fault geometry and slip distribution of the Sarpol Zahab earthquake based on the elastic dislocation theory. Finally, we investigate the Coulomb stress change at a depth of 10 km (the average depth of the aftershocks) derived by the mainshock.

DATA AND INTERPRETATION

The ALOS-2 sensor with radar wavelength of 24.26 cm and Sentinel-1A/1B sensor with wavelength of 5.55 cm capture the SAR images before and after the mainshock of the Sarpol

Table 1 Parameters of Interferometric Pairs of Advanced Land Observation Satellite (ALOS)-2 and Sentinel-1A/1B Synthetic Aperture Radar (SAR) Images					
Sensor	Orbital Path	Acquisition Time (yyyy/mm/dd)	Perpendicular Baseline (m)	Heading Angle (°)	Incidence Angle (°)
ALOS-2	Ascending	Master: 2016/08/09 Slave: 2017/11/14	86.1	351	47.2
	Descending	Master: 2017/10/04 Slave: 2017/11/15			
Sentinel-1	Ascending	Master: 2017/11/12 (S1A) Slave: 2017/11/18 (S1B)	62.2	347	33.8
	Descending	Master: 2017/11/11 (S1A) Slave: 2017/11/17 (S1B)			



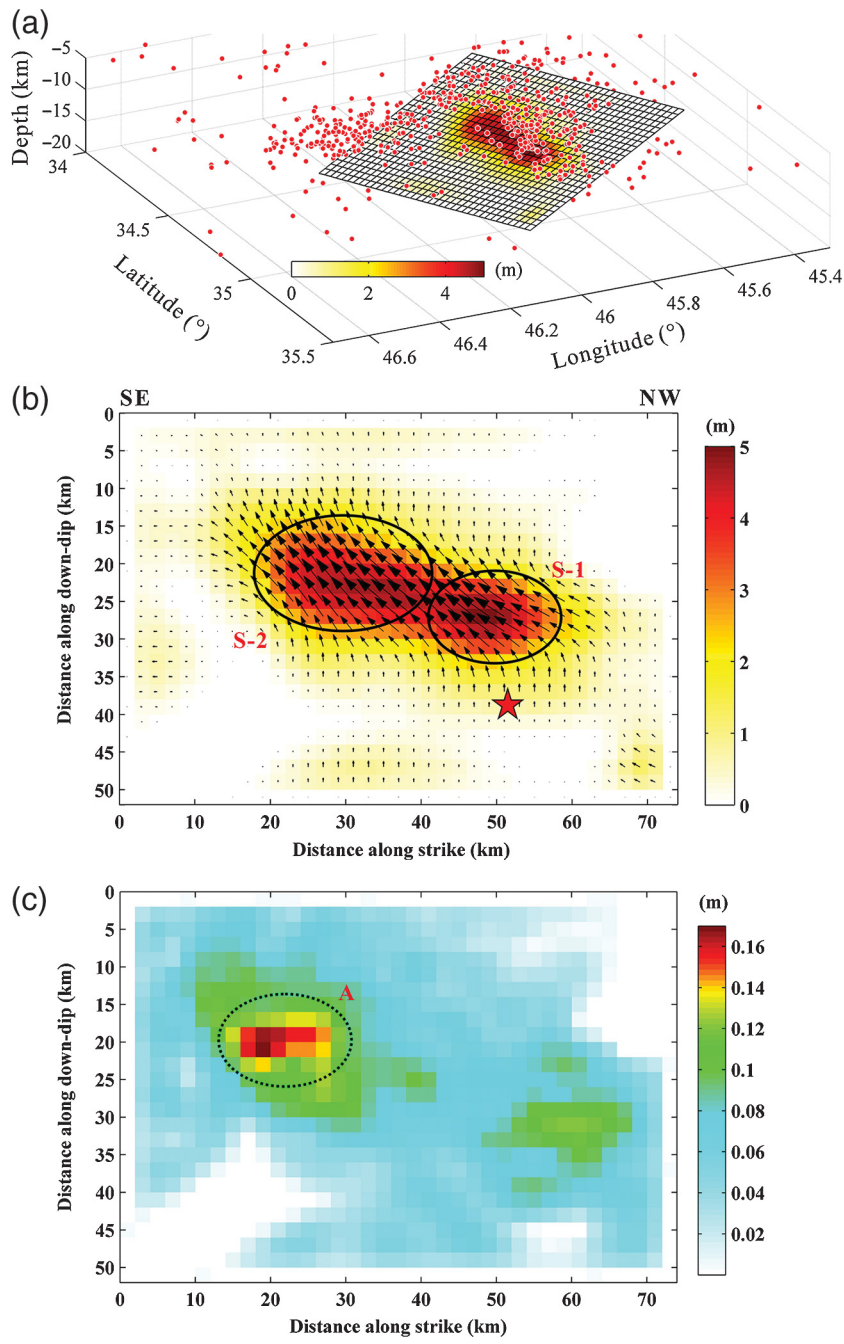
▲ Figure 3. Geologic section cross along the trace of AF (Fig. 1) interpreted from seismic reflection data (modified after Vegrés *et al.*, 2011; Sadeghi and Yassaghi, 2016). Gray circles indicate the relocated seismicity provided by Engdahl *et al.* (2006). The black solid line indicates the inferred fault geometry model in the [Geodetic Modeling](#) section, and the blue dashed ellipse indicates the area with significant fault slip. Red circles represent the aftershocks. HZF, high Zagros fault; KF, Kermanshah fault; MRF, main recent fault; MF, Mar-e-khil fault; RF, Ravansar fault; KHF, Khanequin fault.

Zahab earthquake. To avoid the negative effect on the extracted coseismic InSAR deformation field caused by the post-seismic signal, the observed time of the SAR images nearest the 2017 Sarpol Zahab earthquake is used here. Table 1 and Figure 1 show the detailed information and ground coverage of the used SAR pairs. We exploit two ascending and two descending interferograms derived from both the ALOS-2 and Sentinel-1 satellites to measure the coseismic surface displacements caused by the 12 November 2017 Sarpol Zahab event.

The ascending and descending ALOS-2 scenes acquired in ScanSAR imaging mode are processed using the GAMMA InSAR software (Wegmüller and Werner, 1997). The Shuttle Radar Topography Mission v.4 Digital Elevation Model (SRTM-4 DEM) is introduced to remove the topographic phase component from the original interferogram (Farr *et al.*, 2007). The Sentinel-1 SAR data acquired in the Terrain observation with Progressive Scan (TOPS) imaging mode are processed using the GMTSAR InSAR software, and the topographic component is removed using the SRTM-4 DEM as well. All of the interferograms are unwrapped using the Snaphu software (Chen and Zebker, 2002). We estimate a 2D ramp using the far-field high-coherence (> 0.3) InSAR data and remove it from the initial unwrapped data to mitigate the orbital error, especially for the ALOS-2 data without dense precise orbital vectors (Yang, Chen, Xu, Zhang, Luo, *et al.*, 2017). Figure 3 shows that both the ALOS-2 and Sentinel-1 interferograms maintain the interferometric correlation in

the main seismic zone. We hypothesize that the interferometric decorrelation and some fringe discontinuities within the black dashed ellipses (Fig. 2) should result from the surface motion caused by the shallow fault-related folding in these areas based on the distribution of the faults and shallow folds shown in Figure 3 and [Figure S1](#), available in the electronic supplement to this article (Vegrés *et al.*, 2011; Sadeghi and Yassaghi, 2016).

The ALOS-2 and Sentinel-1 interferograms show that there are not significant phase discontinuities caused by the shallow tectonic faulting over the entire InSAR coverages, which suggests that the coseismic fault rupture has not propagated to the ground surface. Figure 3 shows the InSAR deformation along the geological section along AF shown in Figure 1 and [Figure S1](#). It can be seen from Figures 2 and 3 that both the ascending and descending InSAR deformation fields show two distinguished lobes. One is located at the southwest of the epicenter with positive InSAR deformation in both of the ascending and descending data and indicates that the surface displacement is controlled by the uplift motion in this zone. The other lobe of deformation is located to the northeast of the epicenter where the descending InSAR detecting more significant surface displacements than that of the ascending InSAR. Further considering the surface fault trace presents northwest-southeast direction in this zone; we hypothesize that a buried thrust faulting with northeast dipping could be responsible for the Sarpol Zahab event.



▲ Figure 4. (a) The inferred faulting model and (b) slip error of the 2017 Sarpol Zahab earthquake by the ALOS-2 and Sentinel-1 InSAR observations. Red dots denote the aftershocks from 11 November 2017 to 26 December 2017, black solid ellipses suggest the two high-slip areas, and red dotted ellipse denotes the significant slip error area.

GEODETIC MODELING

We first downsample the initial ascending and descending InSAR deformation fields using uniform sampling algorithm to reduce the computational burden. Then the sampled data with reliable interferometric coherence (> 0.3) are preserved, and 3227 ALOS-2 data and 3079 Sentinel-1 points are used to in-

fer the fault geometry and slip distribution of the 2017 Sarpol Zahab earthquake.

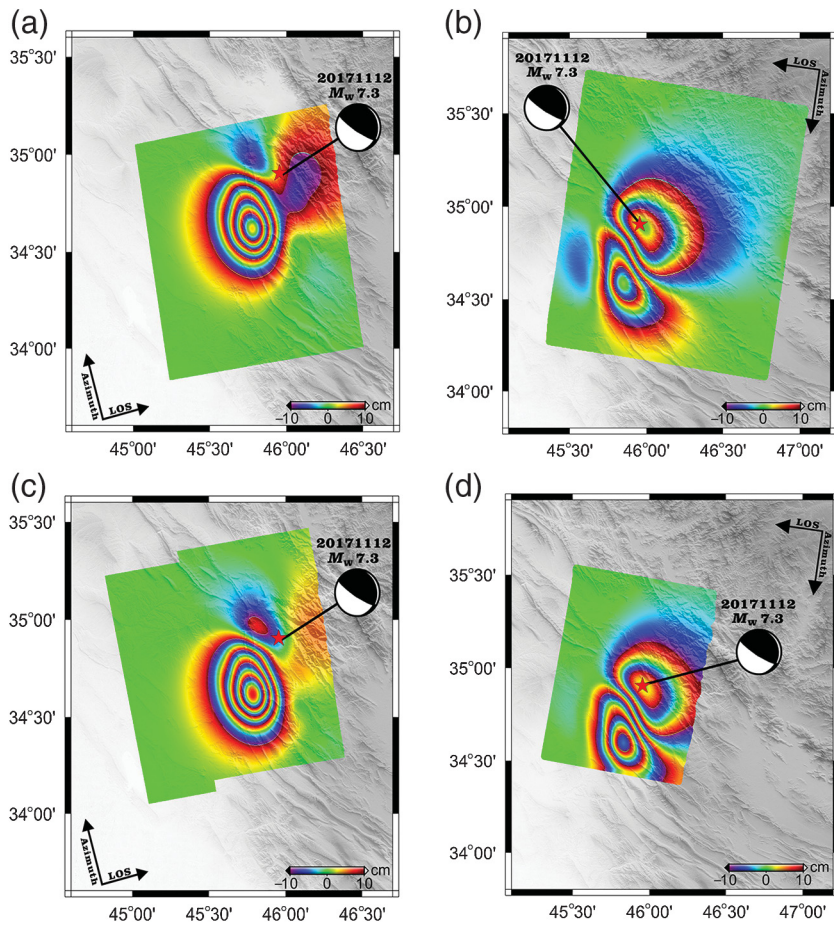
We carry out the geodetic modeling using finite rectangular dislocations in a homogeneous, elastic, and isotropic half-space (Okada, 1985). Considering the possibility that the rupture of a curved fault is responsible for the 2017 Sarpol Zahab earthquake, a flat-ramp fault geometry composed by three individual segments along the down-dip direction is constructed to describe the coseismic fault of the Sarpol Zahab earthquake. The searching range of the flat-ramp fault geometry parameters including strike angle and the up-dip depth of the first subfault segment are respectively set as $[320^\circ, 360^\circ]$, $[-15 \text{ km}, 0 \text{ km}]$ based on the preliminary USGS solution. All the searching ranges of the dip angles of the three subfault segments are set as $[0^\circ, 70^\circ]$. Laplace smoothing constraints are used to regularize the solution and avoid the sharp fault-slip distribution.

The source model inversion is carried out by two-step procedure. First, a nonlinear inversion with large discretization size of $5 \text{ km} \times 5 \text{ km}$. Then the simulated annealing algorithm is used to search the optimal fault geometry parameters, including the azimuth of strike, the depth of the flat-fault segment, and the individual dip angle and width of each subfault segments (Yang, Chen, Xu, Zhang, Yong, et al., 2017; Yang et al., 2018). After that, a linear inversion with small discretization size of $2 \text{ km} \times 2 \text{ km}$ and fixed optimized fault geometry parameters is carried out for inferring the detailed fault-slip distribution of the 2017 Sarpol Zahab earthquake. Moreover, we assess the robustness of the inferred slip distribution by rerunning the inversion for 500 times using a random subset of 85% of the InSAR observation.

RESULTS AND DISCUSSION

The best-fitting fault geometry model shows that the dip angles are 10.8° for the first segment and 11.4° for the second segment, which indicates that there is no significant difference between the dip angles of the above two segments, and thus they could share the same dip angle.

For the third segment, it has a large dip angle of 45.2° ; however, the inferred slip distribution shows there is insignificant fault slip occurred on it (Fig. S2), which suggests the third segment should not be the part of the seismogenic fault. Therefore, it is believed that a fault plane with a single dip angle along the down-dip direction is most likely responsible for the 2017 Sarpol Zahab earthquake. We reperform the searching of the



▲ Figure 5. The predicted InSAR deformation fields of (a) ALOS-2 ascending, (b) ALOS-2 descending, (c) Sentinel-1 ascending, and (d) Sentinel-1 descending by the best-fitting faulting model. The red star indicates the epicenter of the 2017 Sarpol Zahab earthquake.

fault geometry parameter with the assumed configuration of a single fault plane. Using a single fault plane, the final best-fitting fault geometry parameters are 337.5° for the strike angle, 8.5 km for the depth, and 11.2° for the dip angle.

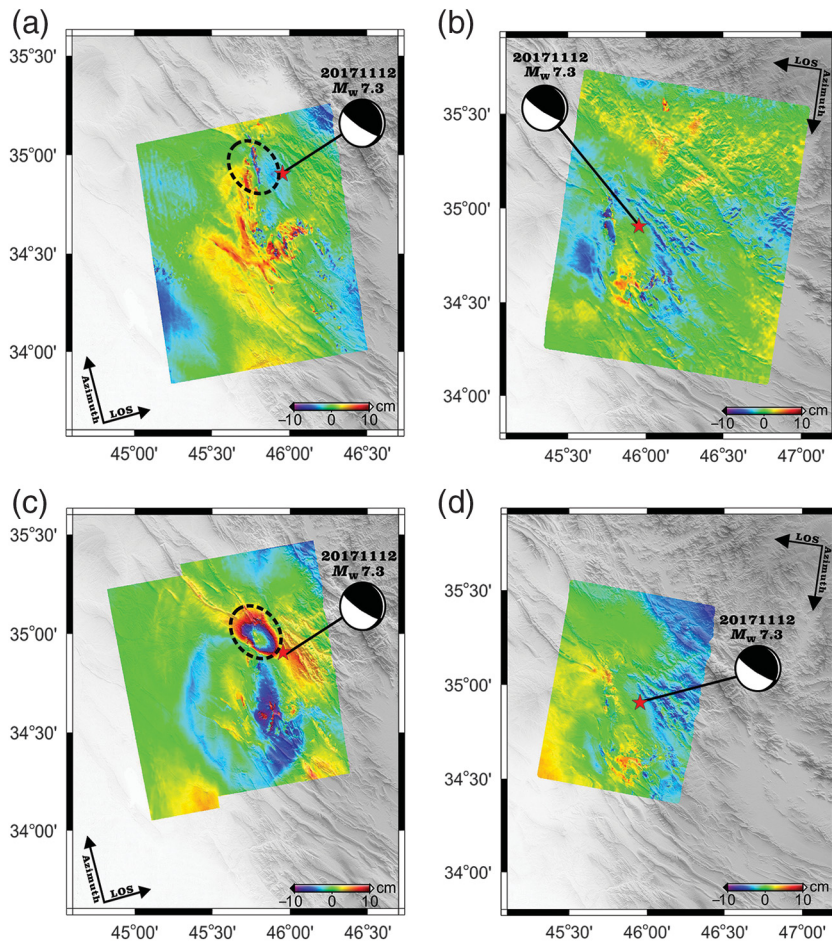
The estimated fault-slip distribution with small discretization size of $2 \text{ km} \times 2 \text{ km}$ by the ascending and descending ALOS-2 and Sentinel-1 InSAR observations based on the optimal single fault geometry parameters is shown in Figure 4. The predicted InSAR deformation derived from the inferred faulting model shows a good fit to the observations of the four InSAR tracks, and the explained ratios (defined in the study by Yang *et al.*, 2018) are $\sim 97.3\%$ and $\sim 98.8\%$, respectively, for the ALOS-2 ascending and descending data and 96.8% and 99.3%, respectively, for the Sentinel-1 ascending and descending data. The model misfits are 2.7 cm of ascending ALOS-2, 1.9 cm of descending ALOS-2, 2.7 cm of ascending Sentinel-1, and 1.3 cm of descending Sentinel-1. Figure 4c demonstrates the slip error distribution, and the significant slip error is located at the area A with an average of 0.17 m. However, the average slip is ~ 4.1 m in the area A and indicates that the slip-to-error ratio is more than 24:1. Therefore, it is believed that the in-

ferred faulting model is sufficiently reliable for the calculation of Coulomb stress change.

The predicted InSAR deformation fields are calculated by the best-fitting fault geometry and slip model and are shown in Figure 5. It is found that both the predicted ALOS-2 and Sentinel-1 InSAR data are consistent with the original observations of Figure 2. The residual fringes within the black dashed ellipses (Fig. 6) could result from the phase unwrapping error and the lack of elastic modeling of the shallow folding that could be anelastic and hydrologic related (Huang *et al.*, 2016). The other residual signals are predominately controlled by the atmospheric delay signal, the unwrapping error, and the surface motion caused by the postseismic afterslip and aftershocks.

From Figures 3 and 4, we find that the main slip is located at the southwest of the epicenter provided by USGS (see Data and Resources), which suggests the fault rupture propagates from the northeast to the southwest. More than 95% of the seismic moment is released at a depth of 11–14 km within the blue dashed ellipse area (Fig. 3). Two slip asperities marked by “S-1” and “S-2” are seen in Figure 4. The S-1 occurs along a strike distance of 40–55 km and at a depth of 11.8–13.5 km with a peak slip of 4.9 m. The S-2 occurs along a strike distance of 15–40 km and at a depth of 10.5–12.5 km with a peak slip of 4.5 m. Both the slip asperities dominantly control the surface deformation shown in Figure 2. There is not any fault slip found above a depth of 10 km, which suggests the coseismic rupture has not transferred through the intervening Hormuz Salt section at a depth of 12–13 km. The seismic moment calculated from our best-fitting faulting model of $1.34 \times 10^{20} \text{ N} \cdot \text{m}$ is equivalent to a moment magnitude of $M_w 7.36$, which is consistent with the USGS solution.

We calculate the Coulomb failure stress (CFS) change caused by the mainshock on the causative fault plane at a depth of 10 km where the mainshock caused the maximum number of the aftershocks. One group of the receiver fault parameters are similar to the mainshock of 337.5° for the strike angle, 11.2° for the dip angle, 90° (Fig. 7c) and 130° (Fig. 7d) for the rake angles, and 0.4 of the friction coefficient. In addition, considering the cross section (Fig. 3) shows that most of the shallow faults and folds have a high dip angle. Consequently, we calculate the CFS change at a depth of 10 km with the receiver parameters characterized by the high dip angle of 75° (the assumed high dip angle estimated by the distributions of the shallow faults and folds shown in Fig. 3), the strike angle of 337.5° , and the rake angles of 90° (Fig. 7a) and 130° (Fig. 7b) for comparison.



▲ Figure 6. The residual InSAR deformation fields of (a) ALOS-2 ascending, (b) ALOS-2 descending, (c) Sentinel-1 ascending, and (d) Sentinel-1 descending between the predicted and observed deformation. Black dashed ellipses indicate the significant InSAR deformation residual areas.

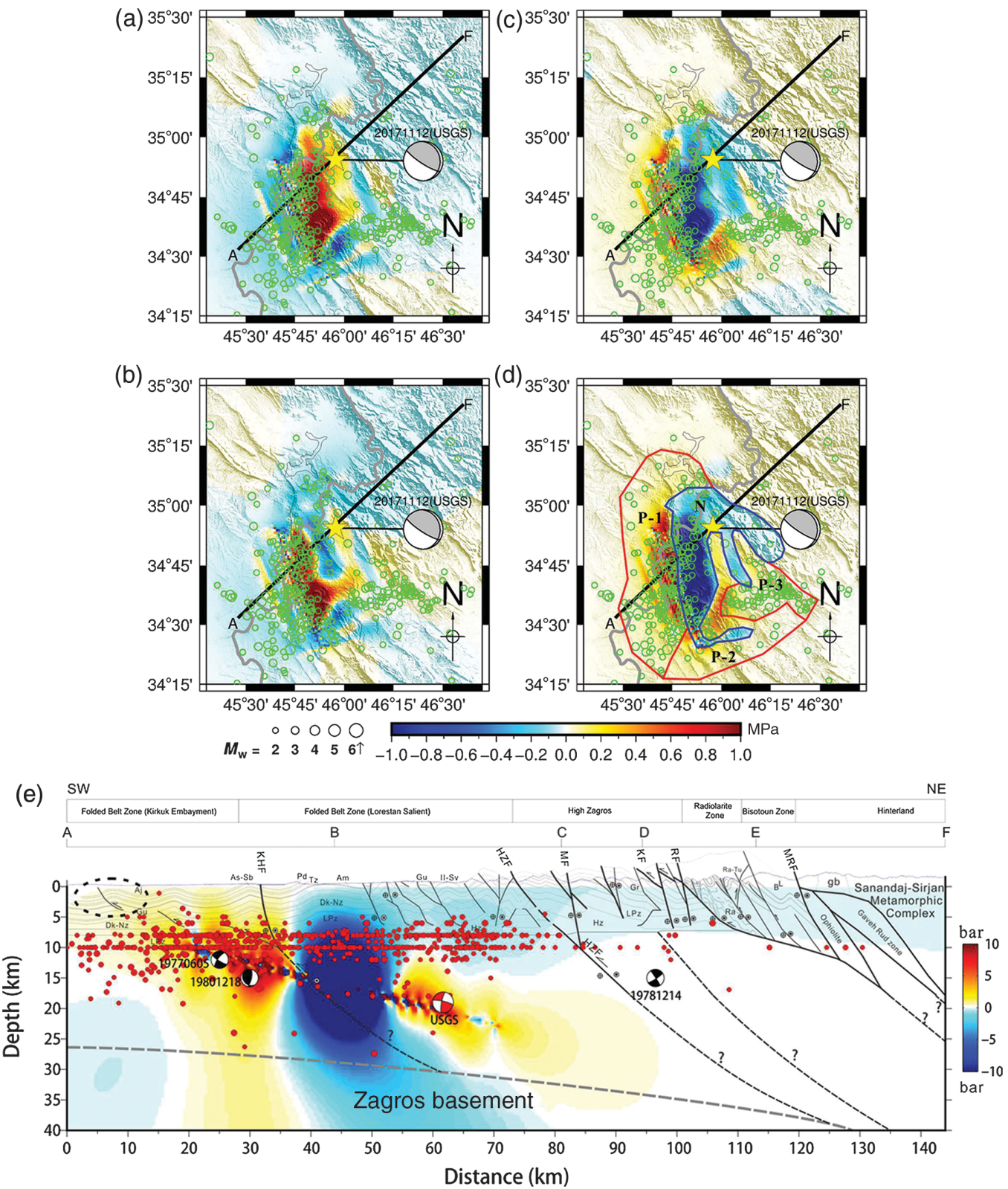
There is not a strong correlation between the positive CFS change and the aftershocks in Figure 7a,b. However, Figure 7d shows a higher consistence between the aftershocks and the positive CFS change than those from Figure 7c, which indicates that most of the aftershocks are characterized by the oblique thrust in the 2017 Sarpol Zahab event. Furthermore, Figure 7d shows that there are three significant positive CFS change areas, which are marked by “P-1,” “P-2,” and “P-3” in Figure 7d, respectively. More than 65% aftershocks occurred in the areas of P-1 and P-3, which suggests that the accumulated stress could have been partly released by the aftershocks in these areas. The average CFS change in the area of P-2 is ~ 3.0 bar, which are sufficient to trigger the rupture if the fault is critically stressed and closed to failure. However, quite few aftershocks occurred following the mainshock in this area, which suggests potential but does not necessitate future event. A good spatial consistency can be found between the high-slip area (Fig. 4) and the area “N” with significant negative CFS change, which is caused by the decrease of the shear stress due to the fault slip. In addition, it is believed that the inconsistency be-

tween the positive CFS change and the aftershocks should be due to comprehensive contributions, including the inaccurate location of the aftershocks, inaccurate receiver fault parameter, and friction coefficient. And whether the aftershocks likely have a similar mechanism to the mainshock needs further test using the focal mechanism of the aftershocks in the future study.

Figure 7e shows the CFS change on the cross section through geologic section AF. It shows that a good number of the aftershocks have occurred in the negative CFS change area at 5- to 12-km depth and along 37- to 80-km distance. We hypothesize that these aftershocks could have occurred because of positive CFS change on a different fault plane in their location. Moreover, the dynamic Coulomb stress change could also partly responsible for the occurrence of these aftershocks (Freed, 2005; Huang et al., 2016). Most of the shallow folds at 35- to 140-km distance experienced negative CFS change, which implies a restraint of the future rupture. The shallow fault-related folding within the black dashed ellipse at 0- to 15-km distance has an average positive CFS change ~ 0.6 bar. The InSAR interferograms (Fig. S3) show that the observed InSAR fringes are discontinuous around this fault-related folding, which indicates that the mainshock has triggered the rupture of this fault.

CONCLUSION

In this study, we first investigated the surface deformation caused by the 2017 Sarpol Zahab earthquake using the ascending, descending InSAR data of the ALOS-2 and Sentinel-1 satellites. Both of the ALOS-2 and Sentinel-1 interferograms maintain the interferometric correlation in the main seismic zone. Then we use the surface displacement data provided by ascending and descending InSAR to estimate the fault geometry model and slip distribution of the mainshock. The best-fitting faulting model shows that a plane fault with low dip angle of 11.2° is responsible for the 2017 Sarpol Zahab earthquake. The inferred slip distribution shows that the fault rupture is concentrated at the 11- to 14-km depth, and the coseismic rupture has not transferred through the intervening Hormuz Salt section at the 12- to 13-km depth. The CFS change indicates that the folds in the southwestern of the main seismic zone have significant positive CFS change, and the InSAR interferograms show that these folds are triggered with aseismic slip by the rupture of the seismogenic fault.



▲ **Figure 7.** The calculated Coulomb stress change at a depth of 10.0 km and along the geologic section of AF by the best-fitting faulting model. The yellow star indicates the location of the mainshock, the black solid line (a-d) shows the surface trace of the geologic section AF, and the black dashed ellipse (e) denotes the triggered shallow fold by the mainshock. The Coulomb failure stress (CFS) change at 10-km depth with receiver parameters of 337.5° for the strike angle, 75° (high dip angle) for the dip angle, and (a) 90° and (b) 135° for the rake angle. The CFS change at 10-km depth with receiver parameters of 337.5° for the strike angle, 11.2° (low dip angle) for the dip angle, and (c) 90° and (d) 135° for the rake angle. The CFS change on a vertical plane through geologic section AF is shown in (e).

DATA AND RESOURCES

Advanced Land Observation Satellite (ALOS)-2 Synthetic Aperture Radar (SAR) images were provided by the Japan Aerospace Exploration Agency (JAXA) under the ALOS-2 RA6 Project (Principal Investigator [PI] Numbers 3314 and 3105) and were processed by the GMTSAR software ([Sandwell et al., 2011](#)). Sentinel-1A SAR images were provided by the European Space Agency (ESA) and were processed by the GAMMA software ([Wegmüller and Werner, 1997](#)). Shuttle Radar Topography Mission v.4 Digital Elevation Model (SRTM DEM) data are the void-filled seamless SRTM data V4, available from the CGIAR-CSI SRTM 90 database (<http://srtm.csi.cgiar.org>, last accessed December 2017). Focal mechanism is provided by the U.S. Geological Survey (USGS), available at <https://earthquake.usgs.gov/earthquakes/eventpage/us2000bmcg#moment-tensor> (last accessed January 2018). Figures were generated using the Generic Mapping Tools (GMT) software ([Wessel and Smith, 1998](#)). 

ACKNOWLEDGMENTS

The comments and suggestions from Associate Editor Brendan Crowell and two anonymous reviewers are deeply appreciated. The authors benefit from fruitful discussions with Ezgi Karasozan, Zhe Su, Morteza Talebian, and Shiann-Jong Lee. Appreciation is also owed to Hsiu-Fang Lee and Hui-Chi Chen, who helped us prepare the figures. This research is supported by the National Key R&D Program of China (2017YFB0502700), the Ministry of Science and Technology in Taiwan under the Grant 106-2116-M-002-004 and the National Natural Science Foundation of China (Numbers 41472255 and 51774250).

REFERENCES

- Alavi, M. (2007). Structures of the Zagros fold-thrust belt in Iran, *Am. J. Sci.* **307**, no. 9, 1064–1095, doi: [10.2475/09.2007.02](https://doi.org/10.2475/09.2007.02).
- Barnhart, W. D., and R. B. Lohman (2013). Phantom earthquakes and triggered aseismic creep: Vertical partitioning of strain during earthquake sequences in Iran, *Geophys. Res. Lett.* **40**, no. 5, 819–823, doi: [10.1002/grl.50201](https://doi.org/10.1002/grl.50201).
- Berberian, M. (1995). Master blind thrust faults hidden under the Zagros folds: Active basement tectonics and surface morphotectonics, *Tectonophysics* **241**, 193–224.
- Berberian, M., and G. C. P. King (1981). Towards a paleogeography and tectonic evolution of Iran, *Can. J. Earth Sci.* **18**, no. 2, 210–265.
- Berberian, M., and R. S. Yeats (2001). Contribution of archaeological data to studies of earthquake history in the Iranian plateau, *J. Struct. Geol.* **23**, 563–584.
- Casciello, E., J. Vergés, E. Saura, G. Casini, N. Fernández, E. Blanc, S. Homke, and D. W. Hunt (2009). Fold patterns and multilayer rheology of the Lurestan Province, Zagros simply folded belt (Iran), *J. Geol. Soc.* **166**, 947–959, doi: [10.1144/0016-76492008-138](https://doi.org/10.1144/0016-76492008-138).
- Chen, C. W., and H. A. Zebker (2002). Phase unwrapping for large SAR interferograms: Statistical segmentation and generalized network models, *IEEE Trans. Geosci. Remote Sens.* **40**, no. 8, 1709–1719, doi: [10.1109/TGRS.2002.802453](https://doi.org/10.1109/TGRS.2002.802453).
- DeMets, C., R. G. Gordon, and D. F. Argus (2010). Geologically current plate motions, *Geophys. J. Int.* **181**, no. 1, 1–80, doi: [10.1111/j.1365-246X.2009.04491.x](https://doi.org/10.1111/j.1365-246X.2009.04491.x).
- Engdahl, E. R., J. A. Jackson, S. C. Myers, E. A. Bergman, and K. Priestley (2006). Relocation and assessment of seismicity in the Iran region, *Geophys. J. Int.* **167**, no. 2, 761–778, doi: [10.1111/j.1365-246X.2006.03127.x](https://doi.org/10.1111/j.1365-246X.2006.03127.x).
- Farr, T. G., P. A. Rosen, E. Caro, R. Crippen, R. Duren, S. Hensley, and D. Seal (2007). The shuttle radar topography mission, *Rev. Geophys.* **45**, no. 2, 1–33, doi: [10.1029/2005RG000183](https://doi.org/10.1029/2005RG000183).
- Freed, A. M. (2005). Earthquake triggering by static, dynamic, and postseismic stress transfer, *Annu. Rev. Earth Planet. Sci.* **33**, 335–367, doi: [10.1146/annurev.earth.33.092203.122505](https://doi.org/10.1146/annurev.earth.33.092203.122505).
- Huang, M.-H., H. Tung, E. Fielding, H.-H. Huang, C. Liang, C. Huang, and J.-C. Hu (2016). Multiple fault slip triggered above the 2016 M_w 6.4 MeiNong earthquake in Taiwan, *Geophys. Res. Lett.* **43**, 7459–7467, doi: [10.1002/2016GL069351](https://doi.org/10.1002/2016GL069351).
- Jackson, J., and T. Fitch (1981). Basement faulting and the focal depths of the larger earthquakes in the Zagros mountains (Iran), *Geophys. J. Int.* **64**, 561–586.
- McQuarrie, N. (2004). Crustal scale geometry of the Zagros fold-thrust belt, Iran, *J. Struct. Geol.* **26**, no. 3, 519–535, doi: [10.1016/j.jsg.2003.08.009](https://doi.org/10.1016/j.jsg.2003.08.009).
- Nissen, E., M. Tatar, J. A. Jackson, and M. B. Allen (2011). New views on earthquake faulting in the Zagros fold-and-thrust belt of Iran, *Geophys. J. Int.* **186**, no. 3, 928–944, doi: [10.1111/j.1365-246X.2011.05119.x](https://doi.org/10.1111/j.1365-246X.2011.05119.x).
- Okada, Y. (1985). Surface deformation to shear and tensile fault in a half-space, *Bull. Seismol. Soc. Am.* **75**, no. 4, 1135–1154.
- Sadeghi, S., and A. Yassaghi (2016). Spatial evolution of Zagros collision zone in Kurdistan, NW Iran: Constraints on Arabia-Eurasia oblique convergence, *Solid Earth* **7**, 659–672, doi: [10.5194/se-7-659-2016](https://doi.org/10.5194/se-7-659-2016).
- Sandwell, D., R. Mellors, X. P. Tong, M. Wei, and P. Wessel (2011). Open radar interferometry software for mapping surface deformation, *Eos Trans. AGU* **92**, no. 28, 234–234.
- Sella, G. F., T. H. Dixon, and A. Mao (2002). REVEL: A model for recent plate velocities from space geodesy, *J. Geophys. Res.* **107**, no. B4, doi: [10.1029/2000JB000033](https://doi.org/10.1029/2000JB000033).
- Sherkati, S., and J. Letouzey (2004). Variation of structural style and basin evolution in the central Zagros (Izeh zone and Dezful embayment), Iran, *Mar. Pet. Geol.* **21**, 535–554, doi: [10.1016/j.marpetgeo.2004.01.007](https://doi.org/10.1016/j.marpetgeo.2004.01.007).
- Stampfli, G. M., and G. D. Borel (2002). A plate tectonic model for the Paleozoic and Mesozoic constrained by dynamic plate boundaries and restored synthetic oceanic isochrons, *Earth Planet. Sci. Lett.* **196**, 17–33, doi: [10.1016/S0012-821X\(01\)00588-X](https://doi.org/10.1016/S0012-821X(01)00588-X).
- Talbot, C. J., and M. Alavi (1996). The past of a future syntaxis across the Zagros, *Geol. Soc. Lond. Spec. Publ.* **100**, no. 1, 89–109, doi: [10.1144/GSL.SP.1996.100.01.08](https://doi.org/10.1144/GSL.SP.1996.100.01.08).
- Talebian, M., and J. Jackson (2004). A reappraisal of earthquake focal mechanisms and active shortening in the Zagros mountains of Iran, *Geophys. J. Int.* **156**, no. 3, 506–526, doi: [10.1111/j.1365-246X.2004.02092.x](https://doi.org/10.1111/j.1365-246X.2004.02092.x).
- Tatar, M., and F. Yamini-Fard (2017). *Seismological Aspects and Aftershock Sequences of the November 12, 2017 Sarpol-e Zahab (Kermanshab) Earthquake ($M_w = 7.3$)*, International Institute of Earthquake Engineering and Seismology IIEES, Tehran, Iran.
- Vegrés, J., E. Saura, E. Casciello, M. Fernández, A. Villaseñor, I. Jiménez-Munt, and D. García-Castellanos (2011). Crustal-scale cross-sections across the NW Zagros belt: Implications for the Arabian margin reconstruction, *Geol. Mag.* **148**, nos. 5/6, 739–761, doi: [10.1017/S0016756811000331](https://doi.org/10.1017/S0016756811000331).
- Vernant, P., F. Nilforoushan, D. Hatzfeld, M. R. Abbassi, C. Vigny, F. Masson, H. Nankali, J. Martinod, A. Ashtiani, R. Bayer, et al. (2004). Present-day crustal deformation and plate kinematics in the Middle East constrained by GPS measurements in Iran and

- northern Oman, *Geophys. J. Int.* **157**, no. 1, 381–398, doi: [10.1111/j.1365-246X.2004.02222.x](https://doi.org/10.1111/j.1365-246X.2004.02222.x).
- Wegmüller, U., and C. Werner (1997). Gamma SAR processor and interferometry software, *Proc. of 3rd ERS Symposium, Space Service Environment (Special Publications 414, ESA)*, Florence, Italy, 14–21 March 1997, Vol. III, 1687–1692.
- Wessel, P., and W. H. F. Smith (1998). New, improved version of Generic Mapping Tools released, *Eos Trans. AGU* **79**, no. 47, 579, doi: [10.1029/98EO00426](https://doi.org/10.1029/98EO00426).
- Yang, Y.-H., Q. Chen, Q. Xu, Y.-J. Zhang, R. Luo, J.-C. Hu, G.-X. Liu, Z.-G. Wang, and J.-Y. Wang (2017). SAR ionosphere signal correction for deformation field of Wenchuan earthquake and extraction of fault surface rupture trace, *Chin. J. Geophys.* **60**, no. 8, 2948–2958, doi: [10.6038/cjg20170804](https://doi.org/10.6038/cjg20170804).
- Yang, Y.-H., Q. Chen, Q. Xu, Y.-J. Zhang, Q. Yong, and G. Liu (2017). Coseismic surface deformation of the 2014 Napa earthquake mapped by Sentinel-1A SAR and accuracy assessment with COSMO-SkyMed and GPS data as cross validation, *Int. J. Digit. Earth* **10**, no. 12, 1197–1213, doi: [10.1080/17538947.2017.1299806](https://doi.org/10.1080/17538947.2017.1299806).
- Yang, Y.-H., M.-C. Tsai, J.-C. Hu, M. A. Aurelio, M. Hashimoto, J. A. P. Escudero, Z. Su, and Q. Chen (2018). Coseismic slip deficit of the 2017 M_w 6.5 Ormoc earthquake that occurred along a creeping segment and geothermal field of the Philippine fault, *Geophys. Res. Lett.* **45**, 2659–2668, doi: [10.1002/2017GL076417](https://doi.org/10.1002/2017GL076417).
- Zare, M., F. Kamranzad, I. Parcharidis, and V. Tsironi (2017). Preliminary report of M_w 7.3 Sarpol-e Zahab, Iran earthquake on November 12, 2017, *EMSC Report*, 1–10.

Ying-Hui Yang¹
Ze-Gen Wang

Department of Remote Sensing and Surveying Engineering
Southwest Petroleum University
No. 8, Xindu Road
Chengdu 610500
Sichuan, China
xzhfhyyy@126.com
zegen01@126.com

Jyr-Ching Hu

Department of Geosciences
National Taiwan University
No. 1, Section 4, Roosevelt Road
Taipei 10617
Taiwan, Republic of China
jchu@ntu.edu.tw

Ali Yassaghi
Department of Geology

Tarbiat Modares University
14117-13116 Tehran, Iran
Yassaghi@modares.ac.ir

Min-Chien Tsai
Seismological Center
Central Weather Bureau
No. 64, Gongyuan Road
Taipei 10048
Taiwan, Republic of China
minchyen@cwb.gov.tw

Mehdi Zare
Farnaz Kamranzad²
Department of Mining Engineering
University of Tehran
1417466191 Tehran, Iran
mzare@iiees.ac.ir
f_kamranzad@ut.ac.ir

Qiang Chen
Department of Remote Sensing and Geoinformation Engineering
Southwest Jiaotong University
No. 111, North 1st Section, 2nd Ring Road
Chengdu 610031
Sichuan, China
swjtucq@sina.com

Ali M. Rajabi
Engineering Geology Department
School of Geology
College of Science
University of Tehran
No.16, Azar Street, Enghelab Square
1417614411 Tehran, Iran
amrajabi@ut.ac.ir

Published Online 10 October 2018

¹ Also at Department of Geosciences, National Taiwan University, No. 1, Section 4, Roosevelt Road, Taipei 10617, Taiwan, Republic of China.

² Also at Swiss Seismological Service, ETH Zürich, CH-8092 Zürich, Switzerland; farnaz.kamranzad@sed.ethz.ch.